*inorganics*

MDPI

*Article*

# Structural and Magneto-Optical Study on the Tetrahedrally Configured [$CoCl_2$(1-allylimidazole)$_2$] and Molecular Docking to Hypoxia-Inducible Factor-1α

**Hela Ferjani [1,*], Bruno Poti e Silva [2], Faizul Azam [3], Yasmeen G. Abou El-Reash [4], Tarek Yousef [4], Nahal Rouzbeh [5], Leonhard Rochels [5], Sabrina Disch [5], Sascha A. Schäfer [6] and Axel Klein [6,*]**

1 Center for Innovation and Entrepreneurship, Imam Mohammad Ibn Saud Islamic University (IMSIU), Riyadh 11623, Saudi Arabia
2 Computational and Quantum Chemistry Group, Instituto Federal de Educação, Ciência e Tecnologia do Ceará, Campus Camocim, Camocim 62400-000, Ceará, Brazil; bruno.poti@fisica.ufc.br or bruno.poti@ifce.edu.br
3 Department of Medicinal Chemistry and Pharmacognosy, College of Pharmacy, Qassim University, Buraydah 51452, Saudi Arabia; f.azam@qu.edu.sa
4 Department of Chemistry, College of Science, Imam Mohammad Ibn Saud Islamic University (IMSIU), Riyadh 11623, Saudi Arabia; ygelreash@imamu.edu.sa (Y.G.A.E.-R.); tayousef@imamu.edu.sa (T.Y.)
5 Faculty of Chemisty and Center for Nanointegration Duisburg-Essen (CENIDE), University of Duisburg-Essen, Universitätsstr. 7, 45141 Essen, Germany; nahal.rouzbeh@uni-due.de (N.R.); leonhard.rochels@uni-due.de (L.R.); sabrina.disch@uni-due.de (S.D.)
6 Institute for Inorganic Chemistry and Materials Chemistry, Department of Chemistry and Biochemistry, Faculty of Mathematics and Natural Sciences, University of Cologne, Greinstrasse 6, 50939 Köln, Germany
* Correspondence: hhferjani@imamu.edu.sa (H.F.); axel.klein@uni-koeln.de (A.K.)

## Abstract

The Co(II) complex [$CoCl_2$(AImd)$_2$] (AImd = 1-allylimidazole) was reinvestigated using a combination of experimental and theoretical methods. The previously reported crystal structure was redetermined and Hirshfeld surface analysis and enrichment ratios were added showing that intermolecular H···Cl and π···π interactions are the primary forces in the crystal structure, while H···H interactions dominate the surface of the molecule, making it rather hydrophobic in keeping with a low solubility in water. A Quantum Theory of Atoms in Molecules (QTAIM)/Non-Covalent Interactions (NCI)-Reduced Density Gradient (RDG) analysis on a dimeric model showed that the energies $V$(r) of the classical H···Cl hydrogen bonds range from −3.64 kcal/mol to −0.75 kcal/mol and were augmented by hydrophobic H···C interactions of >1 kcal/mol. $T$-dependent magnetization measurements reveal paramagnetic behavior with an effective magnetic moment of $\mu_{eff}$ = 4.66(2) $\mu_B$. UV-vis absorption spectra in solution showed intense absorptions peaking at 240 nm, corresponding to intraligand π→π* transitions within the 1-allylimidazole moiety and a structured absorption around 600 nm, which is attributed to the spin-allowed d→d transitions of the high-spin Co(II) $d^7$ ion in a distorted tetrahedral geometry. Both assignments were confirmed through TD-DFT calculations on the electronic transitions and agree with the DFT-calculated compositions of the frontier molecular orbitals. Molecular docking to hypoxia-inducible factor-1 alpha (HIF-1α) gave a docking score of −5.48 kcal/mol and showed hydrophobic···hydrophobic π-stacking interactions with the Ile233, Leu243, Val338, and Leu262 residues. A higher docking score of −6.11 kcal/mol and predominant hydrophobic···hydrophobic interactions with Trp296, His279, and Ile281 were found for HIF-1 inhibiting factor (FIH-1).

**Keywords:** tetrahedral cobalt(II); 1-allylimidazole; magnetism; hydrophobic interactions; docking HIF-1α



Academic Editors: David Morales-Morales, Viviana Reyes-Márquez and Alberto Aragón-Muriel

Received: 8 August 2025
Revised: 17 October 2025
Accepted: 20 October 2025
Published: 23 October 2025

**Citation:** Ferjani, H.; Silva, B.P.e.; Azam, F.; Abou El-Reash, Y.G.; Yousef, T.; Rouzbeh, N.; Rochels, L.; Disch, S.; Schäfer, S.A.; Klein, A. Structural and Magneto-Optical Study on the Tetrahedrally Configured [$CoCl_2$(1-allylimidazole)$_2$] and Molecular Docking to Hypoxia-Inducible Factor-1α. *Inorganics* **2025**, *13*, 344. https://doi.org/10.3390/inorganics13110344

## 1. Introduction

Co(II) complexes have attracted considerable interest because of their interesting structural versatility and applications in molecular magnetism, catalysis, photochemistry, and photophysics [1–6], but also in medicinal chemistry [7–9]. Co(II) with its $d^7$ electron configuration exhibits different coordination geometries, mainly tetrahedral and pseudo-octahedral, influenced by the characteristics of the ligands and crystal packing [2–4,6,10]. This makes Co(II) quite unique, as other $3d^7$-configured metal ions such as Mn(0) or Fe(I) are strong reductants, while Ni(III) is a strong oxidant. The heavier analogues, Rh and Ir, do not stabilize $d^7$ configurations, but are very stable in their M(I) ($d^8$) or M(III) ($d^6$) oxidation states (configurations) [10]. In contrast to the heavier analogues Rh and Ir, the Co(II)/Co(III) redox couple is available in aqueous solution and thus in the biological realm [10,11]. In a biological–medical context, Co(II) is primarily known for its occurrence in coenzyme $B_{12}$ derivatives with hexacoordinated (distorted octahedral) Co(II) containing a macrocyclic corrin ligand, an axial dimethyl-benzimidazole ligand, and another axial alkyl (5′-deoxyadenosyl or methyl) ligand [11]. The tetrahedral coordination preferred by Co(II) is important in studies of biological systems where Co(II) ions were used as paramagnetic probes, substituting Zn(II) in metalloenzymes, which is easily feasible due to their similar ionic radii and coordination characteristics. This substitution facilitates spectroscopic examination of enzyme active sites, frequently preserving enzymatic activity [11,12].

Amongst reported biomedically active Co(II) complexes, $[CoCl_2(L)_2]$ derivatives containing imidazole and benzimidazole ligands (L) form a large group [13–25], which includes $CoCl_2$ complexes of clotrimazole (1-[(2-chlorophenyl)diphenylmethyl]-1*H*-imidazol), an established antifungal agent [22,23], or albendazole (methyl(5-(propylthio)-1*H*-benzimidazol-2-yl)carbamate), which is in use as a broad-spectrum antihelmintic and antiprotozoal agent [13].

In continuation of this work, we studied the Co(II) complex $[CoCl_2(AImd)_2]$ (AImd = 1-allylimidazole) (Scheme 1) that has been previously reported with some structural details and recognized for its anti-hypoxic activity in various hypoxia models [17]. Furthermore, the complex was used as a catalyst for *N*-alkylation of amines with alcohols [19] and its antimicrobial activities were studied along with other alkyl- or propargyl(benz)imidazole $CoCl_2$ complexes [13,15,24,25].

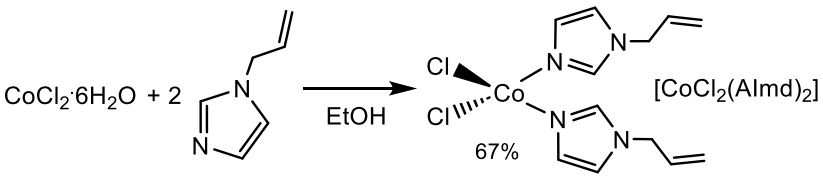


**Scheme 1.** Synthesis of the title complex $[CoCl_2(AImd)_2]$ (AImd = 1-allylimidazole) (**left**) and a photograph of the blue crystalline material (**right**).

In the first part of this report, we will complement the solid-state data of this interesting complex. Specifically, we added Hirshfeld surface analysis and enrichment ratio calculations, Quantum Theory of Atoms in Molecules (QTAIM) and Non-Covalent Interactions (NCI) with Reduced Density Gradient (RDG) on a dimer model, magnetic susceptibility, and UV-vis absorption to the reported single-crystal X-ray structure [17]. Specifically, we probed for molecular properties such as frontier orbital energies and character as well as UV-vis absorptions through a combination of experiment and density functional theory (DFT) and TD-DFT calculation.

As the reported anti-hypoxic properties of $[CoCl_2(AImd)_2]$ [17] were especially interesting to us, we embarked on a molecular docking study using two key hypoxia-related

proteins: hypoxia-inducible factor-1 alpha (HIF-1α) and HIF-1 inhibiting factor (FIH-1). In the second part of this paper, we will report on this to provide deeper insight into relevant biomedical properties and interactions of the title compound.

HIF-1α is a pivotal transcription factor activated under low oxygen conditions, influencing several cellular processes such as angiogenesis, metabolism, and survival [26–28]. Conversely, FIH-1 is an enzyme that negatively regulates HIF-1α activity through hydroxylation, thereby modulating its transcriptional functions. Targeting both proteins can significantly impact cancer treatment strategies by either directly influencing hypoxic responses or modulating the regulators of this pathway [26–32].

The previous study on the anti-hypoxic properties of $[CoCl_2(AImd)_2]$ [17] might have been motivated by an earlier study stating that "nonspecific inhibitors of the HIF hydroxylases, including iron chelating agents, cobaltous ions, {...} have been {...} employed as hypoxia mimetics" in studies of the HIF system. [28]. The report on $[CoCl_2(AImd)_2]$ also fits well with a recent study that showed that $CoCl_2$ can be used to stimulate hypoxia [29], which is in line with the general idea that apart from naturally occurring Fe [28,30–32], other redox-active metals, such as Mn, Co, Ni, Cu, Ru, Os, Rh, or Ir, might play a similar role [28,29,32–41].

In recent years, a number of metal complexes have been studied for their docking to HIF or FIH systems. Recently, a molecular docking study on a series of cyclometalated Rh(III) and Ir(III) complexes of the type $[M(C^N)_2(N^N)]$ or $[M(C^N)_2(MeCN)_2]$, with C^N being cyclometalating ligands of the 2-phenyl-bipyridine type and N^N being bpy and phen-type ligands (bpy = 2,2′-bipyridine, phen = 1,10-phenanthroline), binding on HIF-1α has generated great attention with one example that turned out to stabilize HIF-1α [39,40]. At the same time this complex induced increased gene expression in wound tissue of diabetic mice. An earlier study by the same group targeted Os(II) bpy and phen complexes [38]. The docking study of similar cyclometalated Ir(III) complexes to the Oxidation Resistance 1 (OXR1) protein went into the same direction [41].

For the lighter analogue Co(III)-containing complexes of the type $[Co(L^1)(L^2)]$ with $L^1$ = *N*,*N*-(ethane-1,2-diyl)bis(1-(pyridine-2-yl)methanimine) and $L^2$ = 1-phenyl-1,3-butanedione or dox = doxorubicin, real-time quantitative PCR (RT-PCR) analysis showed downregulation of the key hypoxia-adaptive genes (HIF-1α, VEGF, and GLUT-1) and medium–strong binding to BSA in a very recent molecular docking study [35].

The availability of three-dimensional crystal structures of biological targets from the Protein Data Bank (PDB) and the use of open-source docking simulation platforms such as AutoDock has made such docking studies into a strong tool in drug discovery and development [10,11,18,42–44].

## 2. Results and Discussion

### *2.1. Synthesis and Characterization*

The reaction of $CoCl_2$ $6H_2O$ and 1-allylimidazole (AImd) in a 1:2 ratio in EtOH gave turquoise blue crystals of the complex $[CoCl_2(AImd)_2]$ with an 89% yield, slightly higher than the reported 84% [17]. Elemental analysis confirmed the composition. Fourier-transformed infrared (FT-IR) spectroscopy (Figure S1, Supplementary Materials) agrees with the reported spectrum and assignments [17]. Powder X-Ray diffraction (Figure S2, Supplementary Materials) shows that the material is phase-pure and matches the calculated pattern. Experimental intensities deviate markedly from the calculated pattern, which is probably due to the needle-like morphology [45,46] that was revealed through Scanning Electron Microscopy (SEM) (Figure S3, Supplementary Materials).

Thermogravimetric Analysis (TGA) and Difference Thermogravimetry (DTG) showed stability of $[CoCl_2(AImd)_2]$ (346.12 g/mol) up to 180 °C. Two subsequent mass loss events

at 300 and 470 °C lead to a loss of 31% each, which is equivalent to the loss of both AImd ligands in two separate processes. The residual $CoCl_2$ (129.83 g/mol) decomposes at 650 °C, leaving a residual of 18% of the original mass (Figure S4), which is only a bit more than elemental Co (17%).

The compound was described as air-stable and well soluble in water, EtOH, $CHCl_3$, and DMSO [17]. While we can confirm the stability against oxidation in the solid and in solution, we found a low solubility of about 0.3 mg/mL in water at 298 K. In a 1% saline solution, the solubility was slightly increased to about 0.5 mg/mL as determined through UV-vis absorption spectroscopy.

### 2.2. Structure Description, Hirshfeld Surface and Enrichment Ratio Analysis

The previously reported crystal structure of $[CoCl_2(AImd)_2]$ was confirmed (*P*bca space group, CCDC: 1588359 [17], our determination: 2455508). The molecular structure shows that the Co(II) center is coordinated by two chlorido ligands and two 1-allylimidazole ligands via their N3 atoms, resulting in a distorted tetrahedral geometry (Figure 1) with a $\tau_4$ value of 0.92 [6,17], which is identical to the reported value [17], and points to minor distortions of a perfect tetrahedral configuration ($\tau_4 = 1$) far from a square planar geometry ($\tau_4 = 0$).

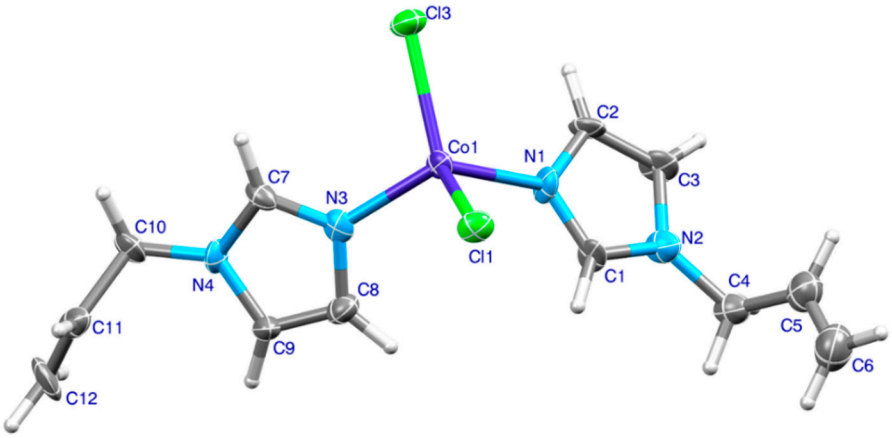


**Figure 1.** The molecular structure of $[CoCl_2(AImd)_2]$ with atomic numbering.

The benzimidazole derivative $[CoCl_2(ABImd)_2]$ (ABImd = 1-allylbenzimidazole)$_2$] showed a $\tau_4$ value of 0.94 [19]. This is even closer to the perfect tetrahedron, but such small differences might be primary due to crystal packing. The Co–Cl and Co–N bond lengths (Table S2) align with expected values for Co(II) in a four-coordinate, tetrahedral environment with chlorido and (benz)imidazole [6,13–21,24,25,47] or pyridine ligands [48–50], whereas the bond angles exhibit minor deviations from the ideal 109.5°. A closer inspection of some related structures shows that crystal packing seems to have a strong impact on the angles around Co, especially N–Co–N and Cl–Co–Cl. For the three benzimidazole complexes $[CoCl_2(RBImd)_2]$ (RBImd = 1-R-benzimidazole; R = vinyl, allyl, and phenylethenyl), the N–Co–N angles range from 104 to 111°, while the Cl–Co–Cl angles vary from 115 to 120° when no steric bulk is imposed by the R substituents [13].

The experimental metrics of $[CoCl_2(AImd)_2]$ were used as an input for the density functional theory (DFT) structure optimization on PBE0-D3/6-311++g(2d,2p) level of theory (in the gas phase) and gave a good match to the calculated and experimental data (Table S3).

The crystal structure shows a three-dimensional network of intermolecular C–H$\cdots$Cl hydrogen bonds, $\pi\cdots\pi$ stacking, and C–H$\cdots\pi$ interactions (Figure 2). The geometric characteristics characterizing these interactions are detailed in Tables S3 and S4, and further structural details are shown in Figures S5–S8.

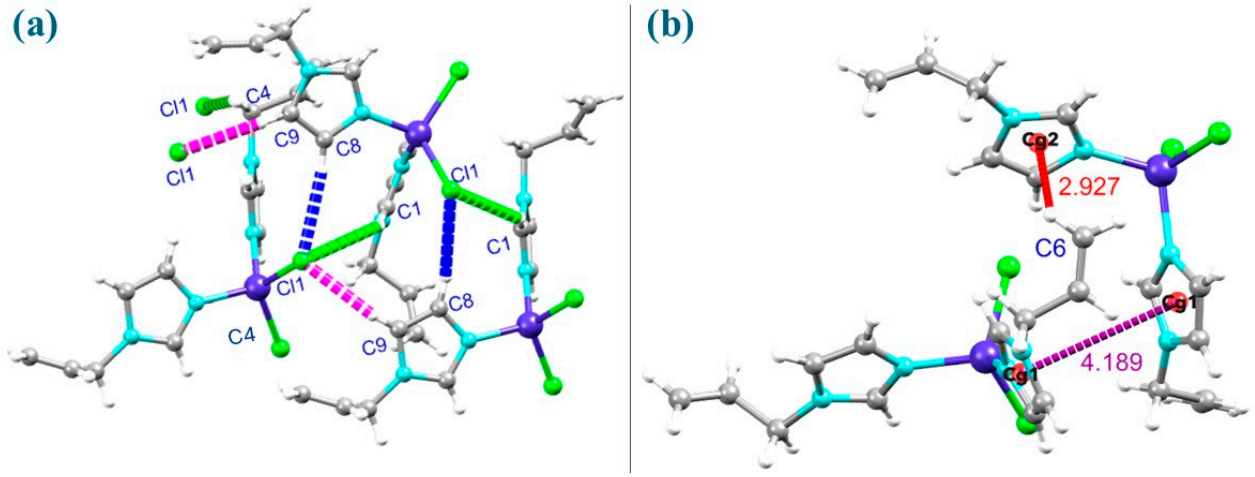


**Figure 2.** (**a**) Hydrogen bonding scheme and (**b**) C–H···π and π···π interactions in $[CoCl_2(AImd)_2]$, with selected distances in Å. C4−H4A···Cl1: 2.79(1) (green dashes), C8−H8···Cl1: 2.73(1) (blue dashes), C9−H9···Cl1: 2.61(1) (magenta dashes), C6−H6···Cg2: 2.927(8), Cg1···$Cg1^{iv}$: 4.189(5), and C–H···$Cg2^{iv}$: 113(1)°. Cg1 and Cg2 are the centroids of the rings N1−C1−N2−C3−C2 and N3−C7−N4−C9−C8, respectively (iv: −1/2+x, y, 3/2−z).

The $d_{norm}$ surface in the Hirshfeld surface analysis revealed close H···Cl/Cl···H contacts (Figure 3, marked in red), representing the C4–H4A···Cl1, C8–H8···Cl1, and C9–H9···Cl1 hydrogen bonds. Both the Shape index (red and blue areas) and the Curvedness on the Hirshfeld surface reveal that C–H···π and π···π interactions are found all over the structure.

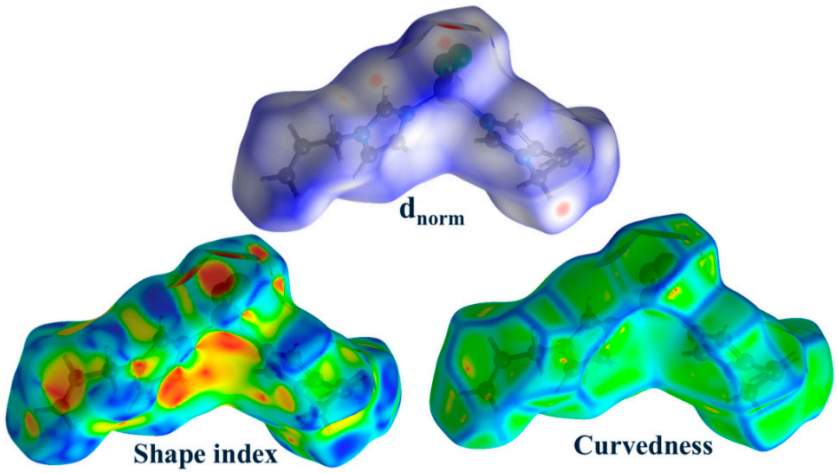


**Figure 3.** Hirshfeld surfaces plotted over $d_{norm}$, shape index, and curvedness for $[CoCl_2(AImd)_2]$.

The 2D fingerprint plots ($d_i$ versus $d_e$) show that H···H contacts are predominating at 45.9% (Figure 4b), followed by Cl···H at 30.0% (Figure 4c), and C···H at 13.2% (Figure 4d). Minor contributions include N···H (5.6%), N···C (2.3%), C···C (1.4%), Co···H (1.2%), and N···N (0.3%) interactions (Table 1).

The enrichment ratios ($E_{XY}$), representing observed intermolecular contact ratios with statistically predicted values [51], show the largest ratio of E = 3.38 for the N···C interaction. This probably means that the π···π-stacking interactions are the superior forces in stabilizing the structure. Likewise, C···C (E = 2.19) and N···N (E = 1.67) interactions were similarly enhanced, indicative of close contact with aromatic or heteroatomic centers.

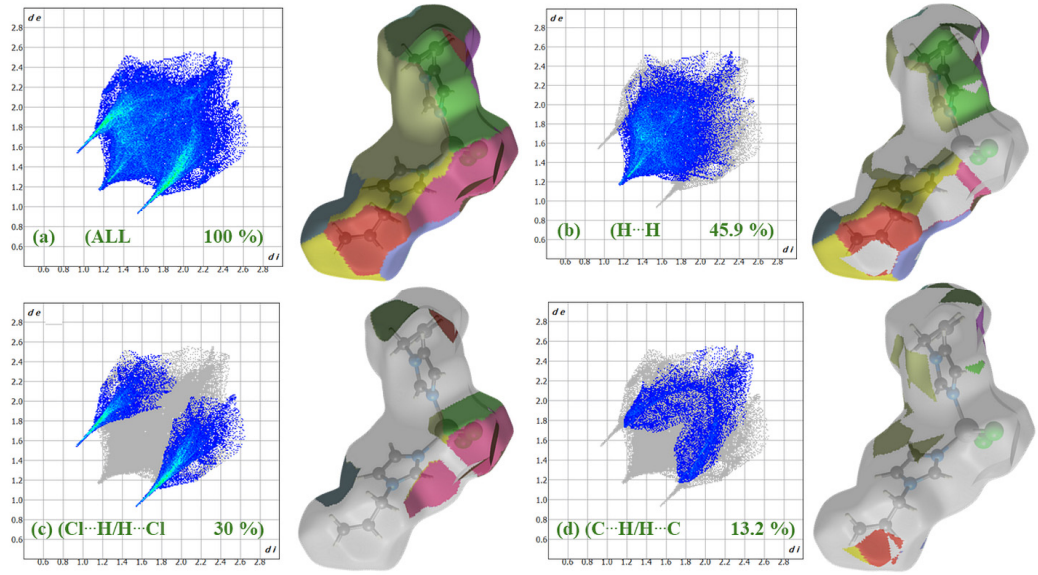


**Figure 4.** Two-dimensional fingerprint plots and their fragment patch surfaces for important contacts in $[CoCl_2(AImd)_2]$, showing (**a**) all interactions, and delineated into (**b**) H···H, and (**c**) H···Cl/Cl···H, and (**d**) C···H/H···C interactions.

**Table 1.** Hirshfeld contact surfaces and enrichment ratios for $[CoCl_2(AImd)_2]$.

| Atoms | H | Cl | C | N | Co |
|---|---|---|---|---|---|
| Surface % | 70.9 | 15 | 8 | 4.25 | 1.2 |
| $E_{XY} = C_{XY}/R_{XY}$ | | | | | |
| Co | 1.41 | - | - | - | - |
| Cl | 1.41 | - | - | - | - |
| N | 0.93 | - | 3.38 | 1.67 | - |
| C | 1.16 | - | 2.19 | 3.38 | - |
| H | 0.91 | 1.41 | 1.16 | 0.93 | 1.41 |

Moderately enriched contacts, such as Cl···H (E = 1.41) and Co···H (E = 1.41), represent the polar interactions between hydrogen atoms and electronegative Cl centers and the metal atom, in accordance with the $d_{norm}$ mapping. C···H interaction shows a minor enrichment (E = 1.16), suggesting the presence of weak hydrogen bonding or dispersive interactions, which are commonly found in crystal systems containing allyl or aromatic groups [52,53]. In contrast, N···H (E = 0.93) and H···H (E = 0.91) interactions were rather small. Overall, the Hirshfeld surface and enrichment ratio show that the crystal packing in this compound is governed by a combination of π···π-stacking N···C and C···C, and hydrogen bonding Cl···H contacts in the crystal lattice.

### *2.3. QTAIM/NCI-RDG Analysis of a Dimer Model of $[CoCl_2(AImd)_2]$*

To improve the understanding of the influence of the interactions in the crystal, the Quantum Theory of Atoms in Molecules (QTAIM), proposed by Bader [54] and Non-Covalent Interactions (NCI) with Reduced Density Gradient (RDG) [55] analysis was performed on a dimeric model of the complex (Figure 5). Only critical points with (σ,λ) = (3,−1) and (3,+3) values in bonds or cages were studied. The topological parameters are summarized in Table S5, Supplementary Materials.

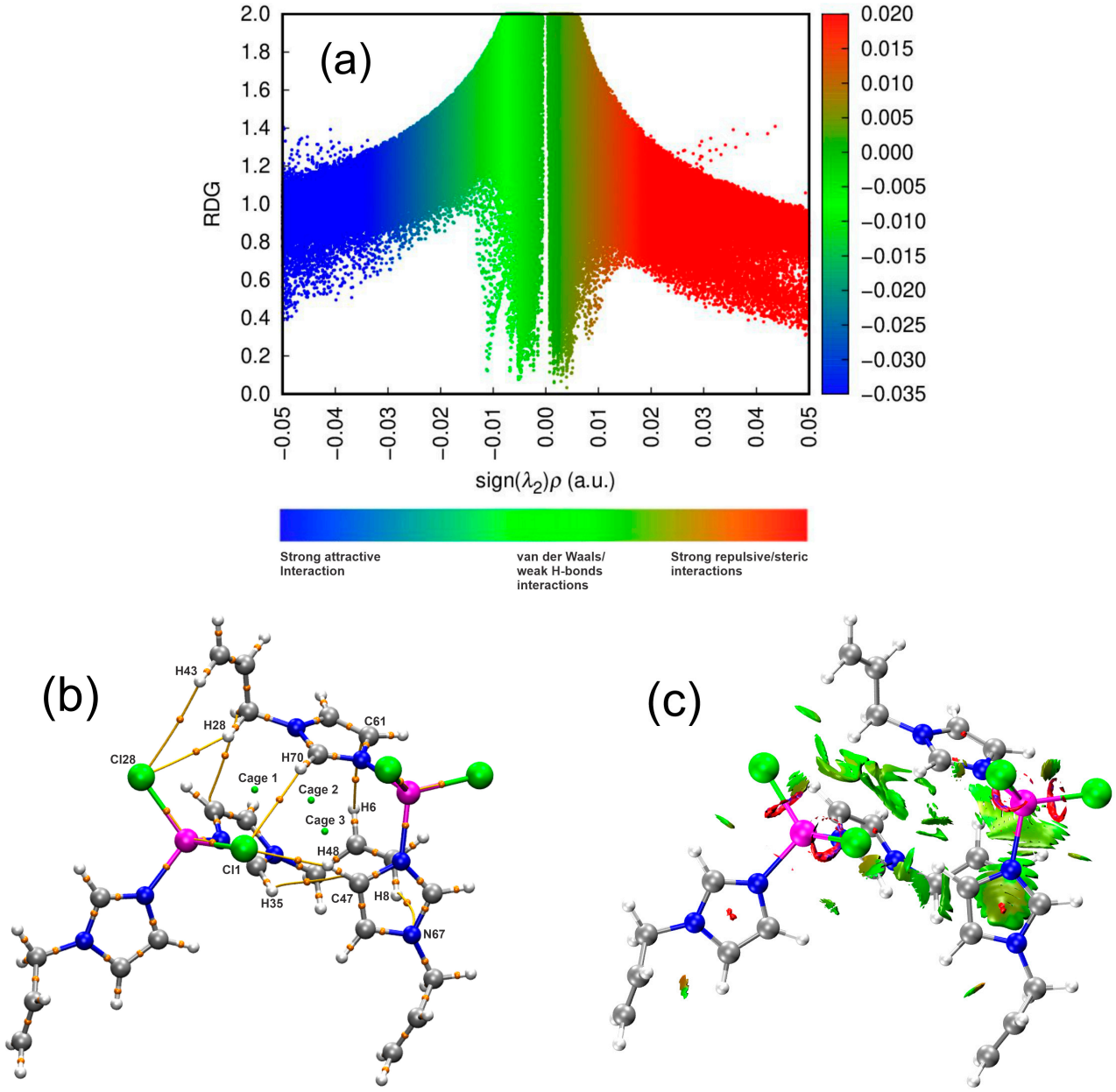


**Figure 5.** (**a**) Reduced density gradient (RDG), (**b**) bond and cage critical points, and (**c**) non-covalent interactions (NCI) analysis of two interacting $[CoCl_2(AImd)_2]$ molecules.

The Laplacian descriptor $|V(r)|/|G(r)|$ describes the nature of the interactions at critical points, where values $|V(r)|/|G(r)| < 1$ are representing van der Waals (vdW) forces/hydrogen bonds and $|V(r)|/|G(r)| > 1$ indicates covalent bonding [56,57]. The hydrogen bonds showed energies $V(r)$ ranging from −3.64 kcal/mol for H48···Cl1 to −0.75 kcal/mol for the H43···Cl28 interaction. At the same time, relatively strong H···C(aromat) interactions are found, with H6···C61 (−1.26 kcal/mol) being the strongest. While these H···Cl interactions are classical donor–H···acceptor interactions, the H6···C(aromat) contacts are typical hydrophobic···hydrophobic interactions. RDG analysis (Figure 5a) shows a concentration of "spikes" in the region near $\rho(r) \approx 0$, showing vdW interactions and weak C–H···Cl and C–H···N hydrogen bonding between the molecules, in line with low $V(r)$ and $H(r)$ values. Moreover, there are cages created by hydrogen bond networks (Figure 5b) with $V(r)$ values between −0.38 and −0.13 kcal/mol. In the NCI analysis (Figure 5c), these cage regions are characterized

by the green isosurfaces, representing the vdW/weak hydrogen bonds between the two interacting $[CoCl_2(AImd)_2]$ molecules.

In summary, the structural study on $[CoCl_2(AImd)_2]$ shows that the individual vdW and hydrogen bonding interactions are only medium to weak, but in sum they have an impact on the crystal lattice energy. The surface of the complex is dominated by H atoms with a surface contribution of about 71% in the 2D fingerprint plots. Thus, both nonpolar and polar van der Waals interactions, as well as hydrogen bonding, are options for intermolecular interactions with other molecules or surfaces. The dominance of H···H contacts with a contribution of about 46% to the overall Hirshfeld surface points to an overall hydrophobic character of the complex. Indeed, solubility in water is very limited (~0.3 mg/mL), while in a 1% saline solution, the solubility is slightly increased (~0.5 mg/mL).

### *2.4. Magnetic Properties*

Temperature-dependent magnetization measurements (Figure 6) reveal nearly perfect paramagnetic behavior in a wide temperature range, as expected for isolated Co(II) centers.

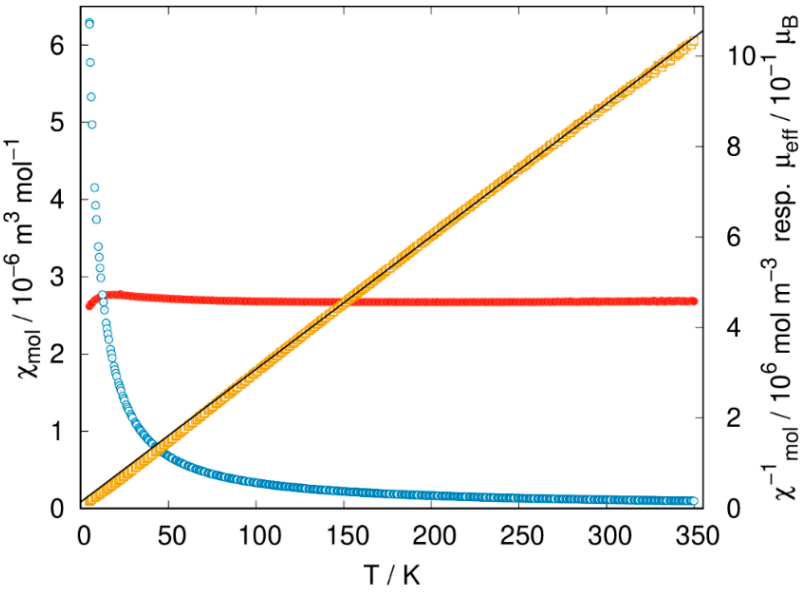


**Figure 6.** Molar susceptibility (blue circles) and inverse molar susceptibility (orange squares) of $[CoCl_2(AImd)_2]$ with fit according to the Curie–Weiss law (black solid line). The red curve represents the effective magnetic moment (in $\mu_B$).

The determined effective magnetic moment of $\mu_{eff}$ = 4.66(2) $\mu_B$ is larger than the spin-only moment of 3.87 $\mu_B$ expected for Co(II) with a $3d^7$ high-spin configuration, indicating significant spin-orbit coupling [58–60]. The recorded value lies in the range from 4.4 to 4.8 $\mu_B$ expected for high-spin tetrahedral Co(II) complexes [58–61] and is in good agreement with reports on similar compounds [2,4,6,50,61–67]. The slight deviation from the linearity of the Curie–Weiss law and the small, negative value of the Weiss constant of −4.9(2) K are attributed to the zero-field splitting effect associated with the $^4A_2$ ground state of tetrahedral Co(II) [47,65,67].

### *2.5. Experimental and TD-DFT-Calculated UV-Vis Absorptions in Solution*

The UV-vis absorption spectra of the $[CoCl_2(AImd)_2]$ complex in EtOH (Figure 7), MeCN, and $CH_2Cl_2$ (Figure S9) solution are very similar and show intense UV-vis bands peaking at 240 nm, which were attributed to intraligand $\pi \rightarrow \pi^*$ transitions within the 1-allylimidazole moiety as the comparison with other AImd complexes shows [52,53,68].

The broad and partially structured band from 500 to 700 is characteristic for spin-allowed d–d transitions of the high-spin Co(II) $d^7$ ion in a distorted tetrahedral geometry [3,65,67,69,70]. In the solid-state spectrum ($BaSO_4$ pellet), the same features were found. The optical band gap $E_g$ was estimated using the Tauc method based on the onset of absorption in the visible region [71], yielding a value of approximately 1.78 eV (Figure S10).

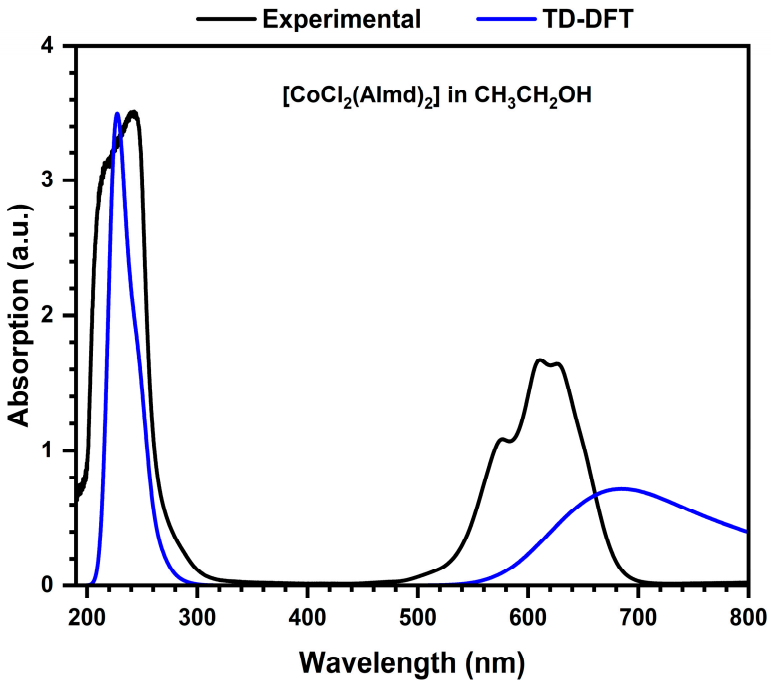


**Figure 7.** Experimental UV-vis absorption spectra of $[CoCl_2(AImd)_2]$ in EtOH solution (black) and TD-DFT-calculated transitions (blue line) on PBE0-D3/6-311++g(2d,2p) level of theory.

The DFT-calculated highest occupied molecular orbital (HOMO) show main contributions of Co (d) and Cl (p) orbitals, and minor admixture of p imidazole orbitals (Figure S11). The lowest unoccupied molecular orbital (LUMO) is exclusively located in the allyl-imidazole π* system.

Time-dependent DFT (TD-DFT) calculations using the solvent polarization (PCM) method, gave excellent agreement of the spectra in EtOH (Figure 7), MeCN, and $CH_2Cl_2$ (Figure S12). The absorptions from 500 to 700 nm are assigned to the $S_0 \rightarrow S_5$ transition (HOMO→LUMO) and the $S_0 \rightarrow S_6$ transition (HOMO–1→LUMO+1) (Table 2, further data in Table S6 ($CH_2Cl_2$) and Table S7 (MeCN)). The character of these transitions is the same in all three solvents and confirms the assumptions that these are essentially d→d* type with small contributions of metal(Co,d)-to-ligand(AImd,π*) charge transfer (MLCT) (Figure 8). The calculated optical energy gap energies are 1.534 eV (in EtOH), 1.525 eV (in $CH_2Cl_2$), and 1.535 eV (in MeCN) and agree well with the experiment.

The absorptions in the UV range can be assigned to the $S_0 \rightarrow S_{14}$ and $S_0 \rightarrow S_{24}$ transitions. Their character depends slightly on the solvent with the main contributions being HOMO–5→LUMO+1 and HOMO–4→LUMO in EtOH, HOMO–4→LUMO+1 and HOMO–4→LUMO in $CH_2Cl_2$, and HOMO–7→LUMO+1, HOMO–5→LUMO+1 and HOMO–4→LUMO+1 in MeCN. These transitions are essentially of π→π* character within the AImd ligands, but they also show marked contributions with MLCT and ligand(Cl, p)-to-ligand(AImd, π*) charge transfer (L'LCT) (Figure 8).

**Table 2.** TD-DFT-calculated $S_0 \rightarrow S_n$ transitions for $[CoCl_2(AImd)_2]$ in EtOH [a].

| State (Wavelength) | osc. Strength | Main Transition | Contribution (%) |
|---|---|---|---|
| $S_5$ (685.34 nm) | 0.0370 | HOMO(β)→LUMO(β) | 52 |
| $S_6$ (667.07 nm) | 0.0040 | HOMO–1(β)→LUMO+1(β) | 52 |
| $S_{14}$ (248.14 nm) | 0.0095 | HOMO–4(β)→LUMO(β) | 68 |
| $S_{24}$ (226.35 nm) | 0.0103 | HOMO–5(β)→LUMO+1(β)/ HOMO–7(β)→LUMO+1(β) | 27/ 18 |

[a] On PBE0-D3/6-311++g(2d,2p) level of theory with EtOH as solvent (PCM). Only contributions with percentage > 15% are listed.

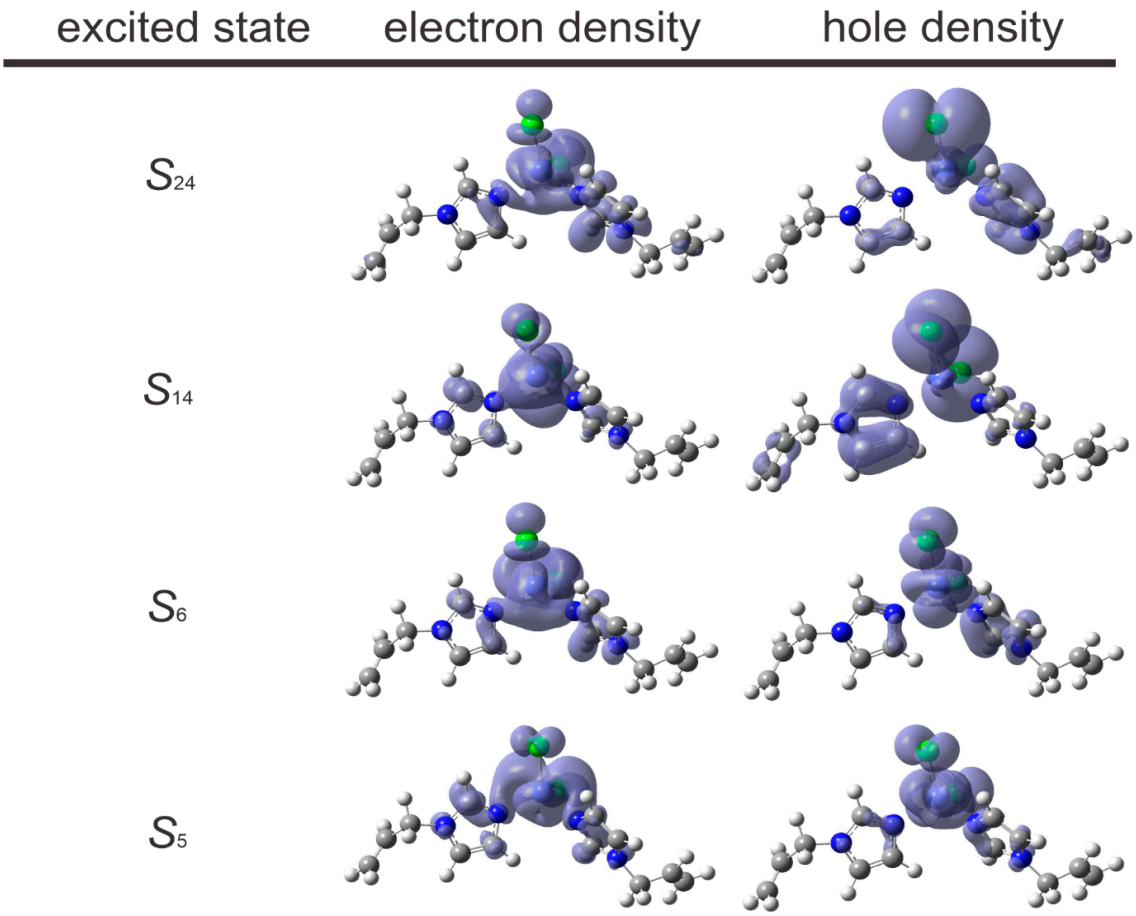


**Figure 8.** TD-DFT-calculated character of $S_0 \rightarrow S_n$ transitions. On PBE0-D3/6-311++g(2d,2p) level of theory with EtOH as solvent (PCM).

### *2.6. Molecular Docking*

Molecular docking analyses were conducted against two important targets involved in the cellular response to hypoxia, hypoxia-inducible factor-1 alpha (HIF-1α) and HIF-1 inhibiting factor (FIH-1). The docking analysis showed that $[CoCl_2(AImd)_2]$ has a moderate binding affinity for HIF-1α, specifically with the hydrophobic residues Ile233, Leu243, Val338, and Leu262 (Figure 9, left). The docking score is −5.48 kcal/mol, indicating stable but modest binding. A notably stronger binding affinity was observed with FIH-1, indicated by a docking score of −6.11 kcal/mol. The complex is found within the active site of FIH-1 and maintains pronounced $\pi \cdots \pi$ interactions with the residues Trp296, His279, and Ile281 (Figure 9, right). This is in line with the rather hydrophobic character of $[CoCl_2(AImd)_2]$ found in our extended structural study.

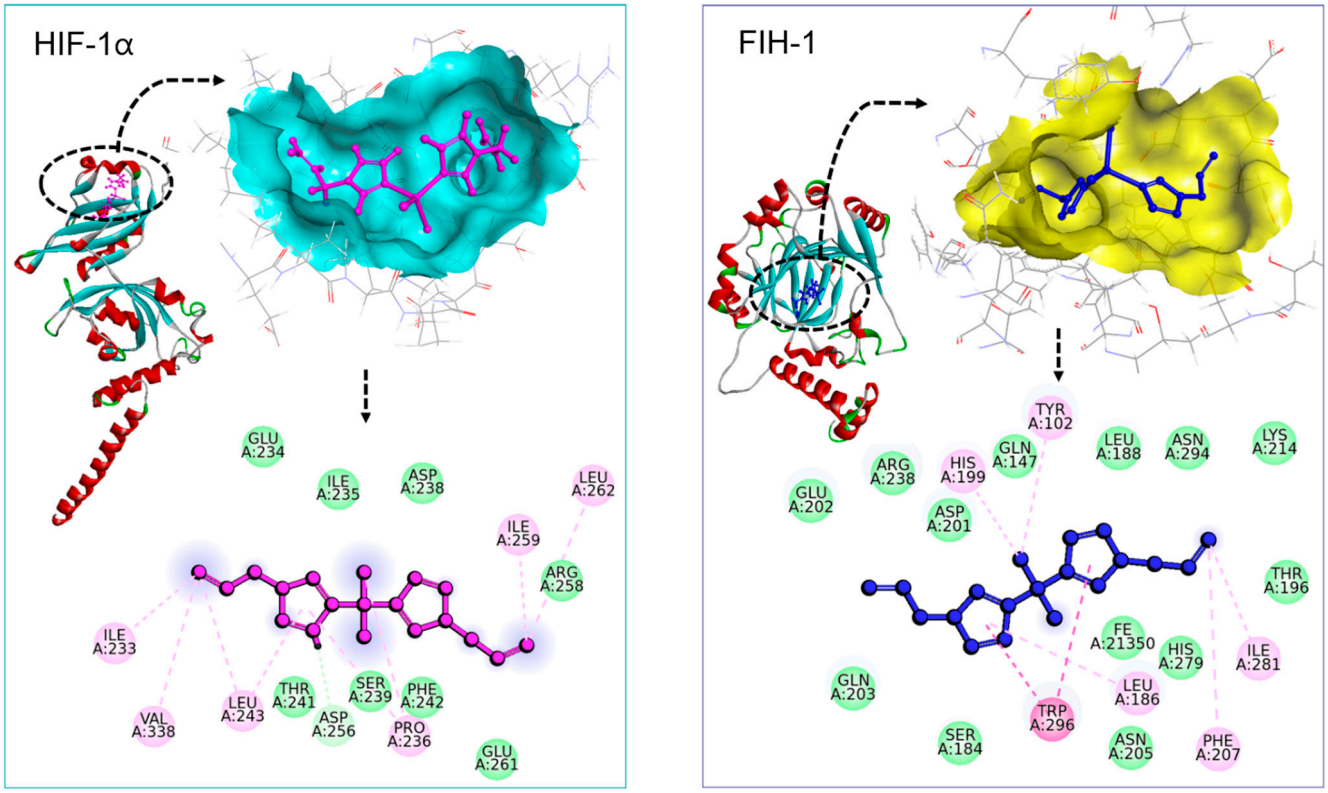


**Figure 9.** Two-dimensional interaction diagrams for the docking of $[CoCl_2(AImd)_2]$ to HIF-1α (PDB ID: 4ZPR) (**Left**) and FIH-1 (PDB ID: 3KCX) (**Right**).

A previous docking study on the very similar $CoCl_2$ complexes $[CoCl_2(1\text{-PImd})_2]$ (1-PImd = 1-propargylimidazole) and $[CoCl_2(ABImd)_2]$ (ABImd = 1-allylbenzimidazole) gave docking scores in the range from −2.5 to −6.7 kcal/mol for selected proteins from pathogens such as *Escherichia coli* (MenB synthase, β-ketoacyl-ACP synthase III, DNA gyrase, topoisomerase II, β-ketoacyl synthase-I, and NAD synthetase), *Bacillus subtilis* (SMC and lipase), and *Staphylococcus aureus* (PBP4, thymidylate kinase, and aldolase) [16]. For $[CoCl_2(ABImd)_2]$, π-stacking interactions were found along with hydrogen bonding [16], which is very similar to our case. For the hexacoordinated $[CoCl_2(PImd)_4]$, a docking score of −4.23 kcal/mol against the thymidylate kinase of *S. aureus* 4QGG was observed, with similar hydrophobic···hydrophobic interactions [18] as we found for the docking of $[CoCl_2(AImd)_2]$ on HIF-1α and FIH-1.

For genistein (4′,5,7-trihydroxyisoflavon), known as angiogenesis inhibitor and phytoestrogen, a docking score of −9.1 kcal/mol and multiple hydrogen bonding to Thr183, Ser184, Asp201, Gln203, and Arg238 was reported [72], while docking of quercetin (3,3′,4′,5,7-pentahydroxyflavon) to HIF-1α gave a score of −8.7 kcal/mol, but a very different hydrogen bonding pattern with main interactions on Asp254, Asp315, Arg383, and His313 [73]. Both values lie below the threshold value of −8.5 kcal/mol that was set for docking scores for potentially interesting HIF-1α inhibitors in a very recent study [74], which means they have slightly stronger binding compared to the minimum requirement suggested by this value.

While the absolute docking score for $[CoCl_2(AImd)_2]$ on HIF-1α of −5.48 kcal/mol lies higher (less negative) than this threshold, the interactions of the hydrophobic Co(II) complex are very different to that of to the hydrophilic isoflavones genistein or quercetin, which are prototypical HIF-1α inhibitors [73,74]. Furthermore, the slightly higher binding affinity to FIH-1 than to HIF-1α suggests that $[CoCl_2(AImd)_2]$ may be able inhibit the hydroxylation activity of FIH-1, thus stabilizing and activating HIF-1α under hypoxic con-

ditions. Consequently, $[CoCl_2(AImd)_2]$ could modulate hypoxia-induced gene expression, promoting beneficial cellular responses such as angiogenesis, metabolic adaptation, and enhanced cell survival. Such activity is particularly relevant in cancer therapeutics, where targeting hypoxia-related pathways can impair tumor progression and improve the efficacy of anticancer treatments [27,72,74]. However, this needs to be studied in future detailed biomedical investigations [75] on the title compound and close derivatives.

An alternative potentially interesting approach towards diabetic wound healing would be to study the interaction of the title compound and close derivatives with the so called Von Hippel–Lindau tumor suppressor protein (VHL) that binds to HIF-1$\alpha$. Inhibition of this interaction would be beneficial to wound healing [76,77] and a recent docking study of an imidazole-pyrazole derivative to VHL confirmed that mimicking HIF-1$\alpha$ is an interesting alternative to interfere with the process of diabetic wound healing [77].

## 3. Materials and Methods

### *3.1. Materials*

The commercially available reagents and solvents $CoCl_2$ $6H_2O$ (99.995%, Sigma-Aldrich, Merck, Darmstadt, Germany), 1-allylimidazole (97%, Fisher Scientific, Schwerte, Germany), $BaSO_4$ (99% ReagentPlus, Merck, Darmstadt, Germany), and absolute EtOH (99.5% GC, Sigma-Aldrich, Merck, Darmstadt, Germany) were used as received.

### *3.2. Synthesis of $[CoCl_2(AImd)_2]$*

A total of 0.33 g (1 mmol) $CoCl_2$ $6H_2O$ and 0.3 g (2 mmol) 1-allylimidazole ($M_W$ = 108.14 g/mol) were dissolved in 25 mL absolute EtOH. The reaction mixture was heated under reflux for 4 h and subsequently allowed to cool to room temperature. Upon cooling, turquoise blue crystals of $[CoCl_2(AImd)_2]$ precipitated, were washed with diethyl ether, and subsequently dried under vacuum. Yield: 89%. Elemental analysis found the following (calc. for $C_{12}H_{16}Cl_2CoN_4$, 346.12 g/mol): C: 41.81 (41.64), H: 4.65 (4.66), and N 16.21 (16.19).

### *3.3. Instrumentation*

The FT-IR spectrum was recorded on a KBr pellet of $[CoCl_2(AImd)_2]$ using a Bruker Tensor 27 FT-IR spectrometer (Bruker, Rheinhausen, Germany). UV-vis absorption in the range from 200 to 700 nm using a JASCO V-770 UV-visible spectrophotometer (JASCO, Pfungstadt, Germany). Solid-state measurements were carried out using single crystals finely ground with $BaSO_4$, and solution spectra were recorded in a 1 cm quartz cuvette. Photoluminescence excitation and emission were recorded at 298 K using a FLS1000 spectrofluorometer (Edinburgh Instruments, Livingston, UK), equipped with a 450 W continuous xenon arc lamp for uninterrupted sample excitation. Magnetization measurements were carried out using the vibrating sample magnetometer (VSM) option of a Quantum Design PPMS Evercool II (Quantum Design, Pfungstadt, Germany). A total of 6.45 mg of sample material was enclosed into a commercially available polypropylene powder sample holder (Quantum Design) and fixed in a brass sample holder. Magnetization measurements were performed in the temperature range from 5 to 350 K with a heating rate of 1 K/min after cooling in an applied magnetic field of 100 mT. The susceptibility data obtained was corrected for a small background signal resulting from the sample holder as determined from reference measurements and for the diamagnetic susceptibility of $\chi_{dia} = -241.08 \times 10^{-11}$ $m^3$ $mol^{-1}$ [78]. A fit of the inverse molar susceptibility data was carried out in the temperature range from 150 to 350 K. The temperature dependence of the effective magnetic moment $\mu_{eff}$ was derived assuming Curie behavior according to $\mu_{eff} = 797.7 \sqrt{\chi T}$ $\mu_B$. Thermogravimetric Analysis (TGA) and Difference Thermogravime-

try (DTG) was conducted using a Mettler Toledo STARe System thermos-microbalance (Mettler-Toledo, Gießen, Germany). The sample was heated in an alumina crucible in a dry $N_2$ atmosphere in the temperature range from 25 to 800 °C at a rate of 5 °C $min^{-1}$.

### *3.4. Single Crystal X-Ray Diffraction*

Single crystal data has been collected using a Bruker (Bruker, Rheinhausen, Germany) X-ray diffractometer (APEX-II CCD, Mo-Kα, λ = 0.71073 Å) at 100 K using APEX2 v2015.5-2 [79]. The structures were solved by dual space methods using SHELXT [80,81] and refinement was carried out with SHELXL 2017 employing full-matrix least-squares methods on $F_0^2 \geq 2\sigma(F_0^2)$ [81,82]. The non-hydrogen atoms were refined with anisotropic displacement parameters without any constraints. The hydrogen atoms were included by using appropriate riding models. Data on the structure solutions and refinements can be obtained under the accession number CCDC 2455508 free of charge at https://www.ccdc.cam.ac.uk/structures/ or from the Cambridge Crystallographic Data Centre, 12 Union Road, Cambridge, CB2 1EZ UK (fax: +44-1223 336033 or e-mail: deposit@ccdc.cam.ac.uk). Selected crystal and structure refinement data are summarized in Table S1 in the Supplementary Materials.

### *3.5. Hirshfeld Surface Analysis and Enrichment Ratio Calculations*

The Crystal Explorer 17.5 program [83] with the TONTO executable was utilized to generate 3D Hirshfeld surfaces and their corresponding 2D fingerprint maps [84,85]. The 3D $d_{norm}$ surfaces are represented on a color scale ranging from −0.26 a.u (red) to 1.26 a.u (blue). The ranges for the shape index and curvedness mapping are from −0.99 to 0.99 Å and −3.299 to 0.26 Å, respectively. The enrichment ratio $E_{XY}$ for a pair of elements (X and Y) is expressed as the ratio of the actual contacts in the crystal ($C_{XY}$) to the theoretical fraction of uniformly distributed random interactions $R_{XY}$ [83,86].

$$E_{XY} = \frac{C_{XY}}{R_{XY}}$$

A pair of elements are likely to create interactions in the crystal if their enrichment ratio exceeds 1, whereas those with an E value below 1 tend to avoid interaction.

### *3.6. DFT Calculations*

DFT geometry optimization was carried out in the gas phase on Gaussian 16 [87] using the PBE0 functional [88] with dispersive forces correction proposed by Grimme (D3) [89] and the 6-311++g(2d,2p) basis set with a threshold convergence of $2 \times 10^6$ Hartree/Å of maximum force with RMS of $1 \times 10^{-6}$ Hartree/Å and maximum displacement of $6 \times 10^{-6}$ Å with RMS of $4 \times 10^{-6}$ Å (1 Hartree converts to 627.5095 kcal/mol). For the DFT-calculated frontier orbitals and the TD-DFT calculations on the UV-vis absorption, the structures were re-calculated using the polarizable continuum method (PCM) [90] for EtOH, $CH_2Cl_2$, and MeCN. The self-consistent field (SCF) calculations were performed with a threshold convergence criterion of $10^{-10}$ Hartree, where quadratically convergent SCF procedure cycles [91] were applied. The TD-DFT results for the UV-vis absorption spectra were analyzed with the GaussSum program [92]. The Multiwfn program [93] was used to analyze orbital composition, where the Hirshfeld method [94] was applied in the calculation of the contributions of individual atoms to the electronic transitions. The QTAIM [54] and NCI-RDG [55] analysis was performed using Multiwfn program [93].

### *3.7. Molecular Docking*

Three-dimensional crystal structures of hypoxia-inducible factor-1 alpha (HIF-1α) and HIF-1 inhibiting factor (FIH-1) were retrieved from the Protein Data Bank (PDB),

using the PDB codes 4ZPR for HIF-1α and 3KCX for FIH-1. Input files for docking were prepared using MGLTools 1.5.7 [95]. Protein structures were initially processed by removing crystallographic water molecules and co-crystal ligands. Missing residues in the HIF-1α protein structure were modeled using Swiss-Model [96], and both protein structures were completed by adding polar H atoms and assigning Gasteiger charges. The structures were then converted into the pdbqt format suitable for docking. Grid boxes for docking were defined based on the active site coordinates as follows: X = −122.894, Y = −51.395, Z = −7.816 for HIF-1α (PDB: 4ZPR), and X = −20.525, Y = 25.483, Z = 7.262 for FIH-1 (PDB: 3KCX). The grid size was consistently set at 40 × 40 × 40 Å for both docking simulations. The geometry of $[CoCl_2(AImd)_2]$ was initially optimized using DFT calculations. Subsequently, Gasteiger charges and rotatable bonds were assigned using MGLTools, and the structure was converted into the pdbqt format. Docking simulations were conducted using AutoDock Vina V1.2.7 [43,44] with an exhaustiveness setting of 100 to ensure thorough exploration of binding conformations. Post-docking analyses involved the visualization and detailed examination of protein···complex interactions to identify critical residues involved in complex binding using the Biovia Discovery Studio Visualizer (Dassault Systèmes, Vélizy-Villacoublay, France). [97].

## 4. Conclusions

Motivated by a recent report that the Co(II) complex $[CoCl_2(AImd)_2]$ (AImd = 1-allylimidazole) showed anti-hypoxic properties, which is potentially interesting for cancer treatment, we reinvestigated this complex using a combination of experimental and theoretical methods with the aim of complementing the existing data on this complex.

We added temperature-dependent magnetization measurements, revealing paramagnetic behavior with an effective magnetic moment of $\mu_{eff}$ = 4.66(2) $\mu_B$. UV-vis absorption spectra in solution showed intense absorptions peaking at 240 nm corresponding to intraligand π→π* transitions within the 1-allylimidazole moiety and a structured absorption around 600 nm, which is attributed to spin-allowed d→d* transitions of the high-spin Co(II) $d^7$ ion in a distorted tetrahedral geometry. Both assignments were confirmed through TD-DFT calculations on the electronic transitions and agree with the DFT-calculated compositions of the frontier molecular orbitals. The solid-state UV-vis absorption spectrum allowed us to determine the optical gap to 1.78 eV using the Tauc plot method, which agrees roughly with TD-DFT-calculated values of about 1.54 eV.

The previously reported sc-XRD structure determination was augmented through a Hirshfeld surface analysis and enrichment ratio study showing that intermolecular H···H contacts dominate the surface of the molecule, while H···Cl and π···π interactions are the primary forces in the crystal structure. Overall, the molecule is expected to show pronounced nonpolar hydrophobic···hydrophobic van der Waals interactions. A Quantum Theory of Atoms in Molecules (QTAIM)/Non-Covalent Interactions (NCI)-Reduced Density Gradient (RDG) analysis on a dimeric model showed hydrogen bond energies $V$(r) ranging from −3.64 kcal/mol for the strongest H···Cl to −0.75 kcal/mol for the weakest H···Cl interaction. At the same time, remarkably strong H···C(aromat) interactions were found, with the strongest having an energy of −1.26 kcal/mol. Classical hydrogen bonding might thus contribute markedly to the crystal structure, but strong hydrogen bonding to surrounding polar molecules is probably disfavored, confirming the hydrophobic nature, in line with the low solubility in water.

Furthermore, we added a molecular docking study on the hypoxia-inducible factor-1 alpha (HIF-1α) and the HIF-1 inhibiting factor (FIH-1), aiming to substantiate the previously reported anti-hypoxic properties of $[CoCl_2(AImd)_2]$. A docking score of −5.48 kcal/mol for HIF-1α and dominating hydrophobic···hydrophobic interactions such as π-stacking

with the Ile233, Leu243, Val338, and Leu262 residues were found in addition to moderate hydrogen bonding. For HIF-1 a higher docking score of −6.11 kcal/mol, and again predominant hydrophobic···hydrophobic interactions with Trp296, His279, and Ile281, was found. Concerning these predominant hydrophobic···hydrophobic interactions, the title complex $[CoCl_2(AImd)_2]$ is similar to previously reported $CoCl_2$ complexes carrying 1-allylbenzimidazole or 1-alkyl or 1-propargylimidazole ligands that showed interesting antimicrobial activities and docking motives. For the anti-hypoxic activity, $[CoCl_2(AImd)_2]$ with a binding energy of –5.48 kcal/mol cannot compete with established HIF-1α inhibitors such as the isoflavones genistein or quercetin that showed markedly higher binding energies in docking studies (−9.1 and −8.5 kcal/mol), but the hydrophobic trait of this complex along with the moderate binding to both HIF-1α and HIF-1 is promising. In future biomedical studies we will further substantiate the potential anti-cancer properties of this and related complexes. As the low solubility of the compound in water is probably an issue for a medical application, another interesting future research direction could be to increase the hydrophilicity of the complex by introducing polar substituents. However, marked changes in the docking interactions might be the consequence.

**Supplementary Materials:** The following supporting information can be downloaded at https://www.mdpi.com/article/10.3390/inorganics13110344/s1: Figure S1: FT-IR spectrum of $[CoCl_2(AImd)_2]$. Figure S2: Experimental vs. simulated PXRD patterns of $[CoCl_2(AImd)_2]$. Figure S3: Scanning electron microscopy (SEM) image of $[CoCl_2(AImd)_2]$. Figure S4: Thermogravimetric analysis and difference thermogravimetry of $[CoCl_2(AImd)_2]$. Figure S5: Perspective view on the crystal structure of $[CoCl_2(AImd)_2]$. Figure S6: Crystal structure of $[CoCl_2(AImd)_2]$ viewed along the crystallographic *a* axis. Figure S7: Crystal structure of $[CoCl_2(AImd)_2]$ viewed along the crystallographic *b* axis. Figure S8: Crystal structure of $[CoCl_2(AImd)_2]$ viewed along the crystallographic *c* axis. Figure S9: DFT-calculated frontier molecular orbital contributions and energy gap $E_g$ for $[CoCl_2(AImd)_2]$ on PBE0-D3/6-311++g(2d,2p) level of theory, calculated with EtOH, $CH_2Cl_2$, or MeCN as solvent. Figure S10: Experimental UV-vis absorption spectra of $[CoCl_2(AImd)_2]$ in the solid state ($BaSO_4$ pellet) and in EtOH, MeCN, and $CH_2Cl_2$ solution. Figure S11: $(\alpha h\upsilon)^2$ over energy (Tauc plot) for determination of the optical bandgap $E_g$ from the solid-state absorption spectrum of $[CoCl_2(AImd)_2]$. Figure S12: Experimental and TD-DFT-calculated UV-vis absorption spectra of $[CoCl_2(AImd)_2]$ in $CH_2Cl_2$ and MeCN calculated at PBE0-D3/6-311++g(2d,2p) level of theory. Table S1: Summary of data collection, structure solution, and structure refinement for $[CoCl_2(AImd)_2]$. Table S2: Geometric parameters for $[CoCl_2(AImd)_2]$. Table S3: Selected experimental and DFT-calculation metrics for $[CoCl_2(AImd)_2]$. Table S4: Hydrogen bond geometry in $[CoCl_2(AImd)_2]$. Table S5: Topological parameters from QTAIM analysis of two $[CoCl_2(AImd)_2]$ molecules. Table S6: TD-DFT-calculated $S_0 \rightarrow S_n$ transitions for $[CoCl_2(AImd)_2]$ in $CH_2Cl_2$. Table S7: TD-DFT-calculated $S_0 \rightarrow S_n$ transitions for $[CoCl_2(AImd)_2]$ in MeCN. Table S8: XYZ coordinates of the DFT-optimized structure of $[CoCl_2(AImd)_2]$ using the PBE0/6-311++g(2d,2p) level of theory in the gas phase.

**Author Contributions:** H.F.: investigation, formal analysis, data curation, resources, methodology, funding acquisition, writing—review and editing, writing—original draft. B.P.e.S. and F.A.: investigation, software, methodology, data curation, writing—original draft, data curation. T.Y. and Y.G.A.E.-R.: investigation, formal analysis, data curation. N.R. and L.R.: investigation, formal analysis, data curation. S.D.: methodology, supervision, formal analysis, data curation, writing—original draft. S.A.S.: methodology, investigation, data curation. A.K.: supervision, writing—review and editing, writing—original draft. All authors have read and agreed to the published version of the manuscript.

**Funding:** This work was supported and funded by the Deanship of Scientific Research at Imam Mohammad Ibn Saud Islamic University (IMSIU) (grant number IMSIU-DDRSP2501).

**Institutional Review Board Statement:** Not applicable.

**Informed Consent Statement:** Not applicable.

**Data Availability Statement:** Data that is not included in the Supplementary Materials will be made available on request.

**Acknowledgments:** The authors acknowledge the general support of the Deanship of Scientific Research at Imam Mohammad Ibn Saud Islamic University (IMSIU). The authors also offer thanks to Tiago Pinheiro Braga of Federal University of Rio Grande do Norte and High Performance Computing Center at UFRN (NPAD/UFRN) for computational resources.

**Conflicts of Interest:** The authors declare that they have no known competing financial interests or personal relationships that could have appeared to influence the work reported in this paper.

## References

1. Stroek, W.; Albrecht, M. Application of First-Row Transition Metal Complexes Bearing 1,2,3-Triazolylidene Ligands in Catalysis and Beyond. *Chem. Soc. Rev.* **2024**, *53*, 6322–6344. [CrossRef]
2. Massoud, S.S.; Mautner, F.A.; Sakiyama, H.; Louka, F.R.; Salem, N.H.M.; Fischer, R.C.; Torvisco, A.; Guizouarn, T.; Velmurugan, G.; Comba, P.; et al. SMM Behavior in Distorted Trigonal Bipyramidal and Tetrahedral Cobalt(II) Complexes Based on Tripodal Tetradentate Phenolic Amines. *Eur. J. Inorg. Chem.* **2025**, *28*, e202400777. [CrossRef]
3. Bielková, Z.; Titiš, J.; Marek, J.; Moncol, J.; Klokočíková, A.; Wesemann, C.; Renz, F.; Rajná, C. Zero-Field Splitting in Tetracoordinate Co(II) Complexes Containing Heterocyclic Aromatic Ligands. *J. Mol. Struct.* **2024**, *1295*, 136667. [CrossRef]
4. Dutta, B.; Guizouarn, T.; Kotrle, K.; Pointillart, F.; Herchel, R.; Ray, D. Tuning Self-Aggregation and Nuclearity in Multinuclear Co(II) Complexes: Synthesis, Structural Diversity, and Changes in Magnetic Anisotropy and Relaxation Behavior. *Cryst. Growth Des.* **2025**, *25*, 3915–3927. [CrossRef]
5. Oleksii, Y.; El-Ghayoury, A. Beyond Spin Crossover: Optical and Electronic Horizons of 2,6-Bis(pyrazol-1-yl)pyridine Ligands and Complexes. *Molecules* **2025**, *30*, 1314. [CrossRef]
6. Sônego Milani, J.L.; Arruda da Mata, A.F.; Santos Oliveira, I.; Mendanha Valdo, A.K.S.; Terra Martins, F.; Rabelo, R.; Cangussu, D.; Cano, J.; Lloret, F.; Julve, M.; et al. Single-molecule magnet behaviour and catalytic properties of tetrahedral Co(II) complexes bearing chloride and 1,2-disubstituted benzimidazole as ligands. *Dalton Trans.* **2022**, *51*, 12258–12270. [CrossRef] [PubMed]
7. Unavane, S.; Patil, R.; Syed, S.; Jain, H.K. Exploring the Therapeutic Potential of Copper and Cobalt Complexes as Anticancer Agents: A Comprehensive Review. *Transit. Met. Chem.* **2025**, *50*, 407–430. [CrossRef]
8. Albobaledi, Z.; Tarahhomi, A.; Khaleghian, A.; van der Lee, A.; Excoffier, G. Novel $Co^{2+}$ and $Cd^{2+}$ Complexes Derived from a New N-Donor Pyridyl-Functionalized Thiophosphoric Triamide Ligand: Structural Investigation, DNA/COVID-19/Monkeypox Molecular Docking, and Biological Assays. *Appl. Organomet. Chem.* **2025**, *39*, e7750. [CrossRef]
9. Chinnasamy, M.; Venkatesh, N.; Marimuthu, P.; Sathiyan, G.; Alharbi, S.A.; Venkatesan, G. Synthesis, Characterization, and Biological Evaluation of Novel Bioactive Schiff Base Metal Complexes and Their Molecular Docking Studies. *J. Environ. Chem. Eng.* **2025**, *13*, 115835. [CrossRef]
10. Gispert, J.R. *Coordination Chemistry*; Wiley-VCH: Weinheim, Germany, 2008; ISBN 978-3-527-31802-5.
11. Kaim, W.; Schwederski, B.; Klein, A. *Bioinorganic Chemistry: Inorganic Elements in the Chemistry of Life—An Introduction and Guide*; John Wiley & Sons, Ltd.: Chichester, UK, 2013; ISBN 978-0-470-97524-4.
12. Borghesani, V.; Zastrow, M.L.; Tolbert, A.E.; Deb, A.; Penner-Hahn, J.E.; Pecoraro, V.L. Co(II) Substitution Enhances the Esterase Activity of a de Novo Designed Zn(II) Carbonic Anhydrase. *Chem.–Eur. J.* **2024**, *30*, e202304367. [CrossRef]
13. Sterkhova, I.V.; Parshina, L.N.; Grishchenko, L.A.; Borodina, T.N.; Belovezhets, L.A.; Semenov, V.A. Metal Complexes of Cobalt Chloride with Vinyl-, Allyl- and Styrylbenzimidazole Ligands: Synthesis, Structure, and Properties. *ChemistrySelect* **2024**, *9*, e202403393. [CrossRef]
14. Daisylet, B.S.; Raphael, S.J.; Kumar, P.; Rajan, P.P.; Dasan, A. Exploring the versatility of sulfur-containing heterocyclic metal complexes: Application in medical and prospects of visible-light-driven photocatalysis. *J. Inorg. Biochem.* **2024**, *257*, 112603. [CrossRef]
15. Sterkhova, I.V.; Parshina, L.N.; Grishchenko, L.A.; Borodina, T.N.; Belovezhets, L.A.; Semenov, V.A. Six-coordinated complexes of Co(II), Ni(II) and Cu(II) chlorides with *N*-propargylimidazoles: Synthesis, structure, antimicrobial activity, AIM analysis and molecular docking. *Polyhedron* **2024**, *260*, 117093. [CrossRef]
16. Yılmaz, Ü.; Apohan, E.; Küçükbay, H.; Yılmaz, Ö.; Tatlıcı, E.; Yesilada, Ö. Synthesis a group of 5(6)-substituted benzimidazole Zn(II) and Co(II) complexes and investigation their cytotoxic and antimicrobial activities. *J. Heterocycl. Chem.* **2022**, *59*, 1241–1246. [CrossRef]
17. Parshina, L.N.; Grishchenko, L.A.; Smirnov, V.I.; Borodina, T.N.; Shakhmardanova, S.A.; Tarasov, V.V.; Apartsin, K.A.; Kireeva, V.V.; Trofimov, B.A. Synthesis, Characterization and Biological Evaluation of Zn(II) and Co(II) Complexes of *N*-Allylimidazole as Potential Hypoxia-Targeting Agents. *Polyhedron* **2019**, *161*, 126–131. [CrossRef]

18. Yılmaz, Ü.; Tekin, S.; Buğday, N.; Yavuz, K.; Küçükbay, H.; Sandal, S. Synthesis and evaluation of anticancer properties of novel benzimidazole ligand and their cobalt(II) and zinc(II) complexes against cancer cell lines A-2780 and DU-145. *Inorg. Chim. Acta* **2019**, *495*, 118977. [CrossRef]
19. Sahin, N.; Yıldırım, I.; Özdemir, N.; Gürbüz, N.; Özdemir, I. First used of Alkylbenzimidazole-Cobalt(II) complexes as a catalyst for the *N*-Alkylation of amines with alcohols under solvent-free medium. *J. Organomet. Chem.* **2020**, *918*, 121285. [CrossRef]
20. Behera, N.; Manivannan, V. Molecular structures of some bivalent metal complexes of 1-(4-acetylphenyl)imidazole and co-ligands. *Polyhedron* **2018**, *149*, 84–94. [CrossRef]
21. Bouchouit, M.; Bouacida, S.; Zouchoune, B.; Merazig, H.; Bua, S.; Bouaziz, Z.; Le Borgne, M.; Supuran, C.T.; Bouraiou, A. Synthesis, X-ray structure, in silico calculation, and carbonic anhydrase inhibitory properties of benzylimidazole metal complexes. *J. Enzyme Inhib. Med. Chem.* **2018**, *33*, 1150–1159. [CrossRef]
22. Betanzos-Lara, S.; Chmel, N.P.; Zimmerman, M.T.; Barrón-Sosa, L.R.; Garino, C.; Salassa, L.; Rodger, A.; Brumaghim, J.L.; Gracia-Mora, I.; Barba-Behrens, N. Redox-active and DNA-binding coordination complexes of clotrimazole. *Dalton Trans.* **2015**, *44*, 3673–3685. [CrossRef]
23. Mahdy, A.R.E.; Ali, O.A.A.; Serag, W.M.; Fayad, E.; Elshaarawy, R.F.M.; Gad, E.M. Synthesis, characterization, and biological activity of Co(II) and Zn(II) complexes of imidazoles-based azo-functionalized Schiff bases. *J. Mol. Struct.* **2022**, *1259*, 132726. [CrossRef]
24. Sahin, N.; Üstün, E.; Özdemir, I.; Günal, S.; Özdemir, N.; Bülbül, H.; Gürbüz, N.; Özdemir, I.; Sémeril, D. Antimicrobial activities of bis-(*N*-alkylbenzimidazole)-cobalt(II) and zinc(II) complexes. *Inorg. Chem. Commun.* **2023**, *157*, 111396. [CrossRef]
25. Sterkhova, I.V.; Parshina, L.N.; Grishchenko, L.A.; Borodina, T.N.; Belovezhets, L.A.; Semenov, V.A. Synthesis, Structure, and Antimicrobial Properties of New Cobalt(II) Complexes with 1-Propargylimidazoles. *Curr. Org. Chem.* **2024**, *28*, 708–715. [CrossRef]
26. Masoud, G.N.; Li, W. HIF-1α pathway: Role, regulation and intervention for cancer therapy. *Acta Pharm. Sin. B* **2015**, *5*, 378–389. [CrossRef]
27. Shi, Y.; Lin, X.; Wang, J.; Zhou, Z.; Chen, S.; Chen, G. Advances of HIF-1α/glycolysis axis in non-small cell lung cancer (Review). *Oncol. Rep.* **2024**, *51*, 55. [CrossRef]
28. Tian, Y.-M.; Yeoh, K.K.; Lee, M.K.; Eriksson, T.; Kessler, B.M.; Kramer, H.B.; Edelmann, M.J.; Willam, C.; Pugh, C.W.; Schofield, C.J.; et al. Differential Sensitivity of Hypoxia Inducible Factor Hydroxylation Sites to Hypoxia and Hydroxylase Inhibitors. *J. Biol. Chem.* **2011**, *286*, 13041–13051. [CrossRef]
29. Bahadori, M.B.; Vandghanooni, S.; Dinparast, L.; Eskandani, M.; Ayatollahi, S.A.; Ata, A.; Nazemiyeh, H. Triterpenoid corosolic acid attenuates HIF-1 stabilization upon cobalt (II) chloride-induced hypoxia in A549 human lung epithelial cancer cells. *Filoterapia* **2019**, *134*, 493–500. [CrossRef] [PubMed]
30. Corner, T.P.; Teo, R.Z.R.; Wu, Y.; Salah, E.; Nakashima, Y.; Fiorini, G.; Tumber, A.; Brasnett, A.; Holt-Martyn, J.P.; Figg, W.D., Jr.; et al. Structure-guided optimisation of *N*-hydroxythiazole-derived inhibitors of factor inhibiting hypoxia-inducible factor-α. *Chem. Sci.* **2023**, *14*, 12098–12120. [CrossRef]
31. Yadav, P.K.; Singh, S.; Singh, A.K. '3D-QSAR-based, pharmacophore modelling, virtual screening, and molecular docking studies for identification of hypoxia-inducible factor-1 inhibitor with potential bioactivity. *Comp. Biol. Med.* **2023**, *166*, 107557. [CrossRef] [PubMed]
32. Yeoh, K.K.; Chan, M.C.; Thalhammer, A.; Chowdhury, M.D.R.; Tian, Y.-M.; Stolze, I.; McNeill, L.A.; Lee, M.K.; Woon, E.C.Y.; Mackeen, M.M.; et al. Dual-action inhibitors of HIF prolyl hydroxylases that induce binding of a second iron ion. *Org. Biomol. Chem.* **2013**, *11*, 732–745. [CrossRef] [PubMed]
33. Jagathesan, K.; Roy, S. Recent Development of Transition Metal Complexes as Chemotherapeutic Hypoxia Activated Prodrug (HAP). *ChemMedChem* **2024**, *19*, e202400127. [CrossRef]
34. Xue, J.-J.; Chen, Q.-Y.; Kong, M.-Y.; Zhu, C.-Y.; Gen, Z.-R.; Wang, Z.-L. Synthesis, cytotoxicity for mimics of catalase: Inhibitors of lactate dehydrogenase and hypoxia inducible factor. *Eur. J. Med. Chem.* **2014**, *80*, 1–7. [CrossRef]
35. Wahengbam, S.; Sharma, H.; Chanu, P.R.; Masarkar, N.; Mukherjee, S.; Menon, M.B.; Malakar, C.C.; Roy, M. Bio-reductive Co(III)–doxorubicin complex for cancer cell-selective delivery of doxorubicin and potent anticancer activity. *RSC Med. Chem.* **2025**, online. [CrossRef]
36. Ke, Q.; Kluz, T.; Costa, M. Down-Regulation of the Expression of the FIH-1 and ARD-1 Genes at the Transcriptional Level by Nickel and Cobalt in the Human Lung Adenocarcinoma A549 Cell Line. *Int. J. Environ. Res. Public Health* **2005**, *2*, 10–13. [CrossRef]
37. Sun, L.; Ding, X.; Kang, Y.J. ABCE1 selectively promotes HIF-1α transactivation of angiogenic gene expression. *J. Trace Elem. Med. Biol.* **2023**, *80*, 127307. [CrossRef] [PubMed]
38. Yang, C.; Wang, W.; Li, G.-D.; Zhong, H.-J.; Dong, Z.-Z.; Wong, C.-Y.; Kwong, D.W.J.; Ma, D.-L.; Leung, C.-H. Anticancer osmium complex inhibitors of the HIF-1α and p300 protein-protein interaction. *Sci. Rep.* **2017**, *7*, 42860. [CrossRef] [PubMed]

39. Li, G.; Li, D.; Wu, C.; Li, S.; Chen, F.; Peng Li, P.; Ko, C.-N.; Wang, W.; Lee, S.M.-Y.; Lin, L.; et al. Homocysteine-targeting compounds as a new treatment strategy for diabetic wounds via inhibition of the histone methyltransferase SET7/9. *Nat. Exp. Mol. Med.* **2022**, *54*, 988–998. [CrossRef]
40. Li, G.; Ko, C.-N.; Li, D.; Yang, C.; Wang, W.; Yang, G.-J.; Di Primo, C.; Wong, V.K.W.; Xiang, Y.; Lin, L.; et al. A small molecule HIF-1α stabilizer that accelerates diabetic wound healing. *Nat. Commun.* **2021**, *12*, 3363. [CrossRef] [PubMed]
41. Peng, C.; Luo, J.; Wang, K.; Li, J.; Ma, Y.; Li, J.; Yang, H.; Chen, T.; Zhang, G.; Ji, X.; et al. Iridium metal complex targeting oxidation resistance 1 protein attenuates spinal cord injury by inhibiting oxidative stress-associated reactive oxygen species. *Redox Biol.* **2023**, *67*, 102913. [CrossRef]
42. Che, X.; Liu, Q.; Zhang, L. An accurate and universal protein-small molecule batch docking solution using Autodock Vina. *Res. Engin.* **2023**, *19*, 101335. [CrossRef]
43. Eberhardt, J.; Santos-Martins, D.; Tillack, A.F.; Forli, S. AutoDock Vina 1.2.0: New Docking Methods, Expanded Force Field, and Python Bindings. *J. Chem. Inf. Model.* **2021**, *61*, 3891–3898. [CrossRef]
44. Trott, O.; Olson, A.J. AutoDock Vina: Improving the speed and accuracy of docking with a new scoring function, efficient optimization, and multithreading. *J. Comput. Chem.* **2010**, *31*, 455–461. [CrossRef]
45. Sherwood, A.M.; Kargbo, R.B.; Kaylo, K.W.; Cozzi, N.V.; Meisenheimer, P.; Kaduk, J.A. Psilocybin: Crystal Structure Solutions Enable Phase Analysis of Prior Art and Recently Patented Examples. *Acta Crystallogr. C* **2022**, *78*, 36–55. [CrossRef] [PubMed]
46. Bergese, P.; Bontempi, E.; Colombo, I.; Depero, L.E. Micro X-ray Diffraction on Capillary Powder Samples: A Novel and Effective Technique for Overcoming Preferred Orientation. *J. Appl. Crystallogr.* **2001**, *34*, 663–665. [CrossRef]
47. Pınar, S.; Akkurt, M.; Kücükbay, H.; Orhan, E.; Büyükgüngör, O. Bis[1-(but-2-enyl)-5-nitro-1*H*-benzimidazole-κ$N^3$]-dichlorocobalt(II). *Acta Crystallogr. E Struct. Rep.* **2006**, *62*, m1663–m1665. [CrossRef]
48. Vershinin, M.A.; Adonin, S.A. Crystal Structure of $CoCl_2{\cdot}6H_2O$ Reaction Products with 2-Methylpyridine and 2,6-Dimethylpyridine. *J. Struct. Chem.* **2021**, *62*, 90–94. [CrossRef]
49. Adonin, S.A.; Bondarenko, M.A.; Novikov, A.S.; Sokolov, M.N. Halogen Bonding in Isostructural Co(II) Complexes with 2-Halopyridines. *Crystals* **2020**, *10*, 289. [CrossRef]
50. Ahmadi, R.A.; Safari, N.; Khavasi, H.R.; Amani, S. Four new Co(II) complexes with 2-amino-4-methylpyridine, 2-amino-3-methylpyridine, or 2-amino-5-chloropyridine: Synthesis, spectroscopy, magnetic properties, and crystal structure. *J. Coord. Chem.* **2011**, *64*, 2056–2065. [CrossRef]
51. Jelsch, C.; Ejsmont, K.; Huder, L. The enrichment ratio of atomic contacts in crystals, an indicator derived from the Hirshfeld surface analysis. *IUCrJ* **2014**, *1*, 119–128. [CrossRef]
52. Ferjani, H. Structural, Hirshfeld Surface Analysis, Morphological Approach, and Spectroscopic Study of New Hybrid Iodobismuthate Containing Tetranuclear 0D Cluster $Bi_4I_{16}{\cdot}4(C_6H_9N_2){\cdot}2(H_2O)$. *Crystals* **2020**, *10*, 397. [CrossRef]
53. Ferjani, H.; Lemine, O.M.; Ben Smida, Y.; Salah, N.; Kaouach, H.; Saadi, F.; Wahbi, H.I.; Almashnowi, M.Y.; Ramadan, R.; Onwudiwe, D.C. Visible Emission from a Zero-Dimensional Tin-Based Organic–Inorganic Metal Halide for Luminescent Devices: Experimental and Theoretical Investigation. *J. Mol. Struct.* **2025**, *1327*, 141210. [CrossRef]
54. Bader, R.F.W. A quantum theory of molecular structure and its applications. *Chem. Rev.* **1991**, *91*, 893–928. [CrossRef]
55. Johnson, E.R.; Keinan, S.; Mori-Sánchez, P.; Contreras-García, J.; Cohen, A.J.; Yang, W. Revealing Noncovalent Interactions. *J. Am. Chem. Soc.* **2010**, *132*, 6498–6506. [CrossRef]
56. Espinosa, E.; Alkorta, I.; Elguero, J.; Molins, E. From weak to strong interactions: A comprehensive analysis of the topological and energetic properties of the electron density distribution involving X–H···F–Y systems. *J. Chem. Phys.* **2002**, *117*, 5529–5542. [CrossRef]
57. Espinosa, E.; Alkorta, I.; Rozas, I.; Elguero, J.; Molins, E. About the evaluation of the local kinetic, potential and total energy densities in closed-shell interactions. *Chem. Phys. Lett.* **2001**, *336*, 457–461. [CrossRef]
58. Murrie, M. Cobalt(II) single-molecule magnets. *Chem. Soc. Rev.* **2010**, *39*, 1986–1995. [CrossRef]
59. Ostrovsky, S.; Tomkowicz, Z.; Haase, W. High-spin Co(II) in monomeric and exchange coupled oligomeric structures: Magnetic and magnetic circular dichroism investigations. *Coord. Chem. Rev.* **2009**, *253*, 2363–2375. [CrossRef]
60. Murray, K.S. Advances in Polynuclear Iron(II), Iron(III) and Cobalt(II) Spin-Crossover Compounds. *Eur. J. Inorg. Chem.* **2008**, *2008*, 3101–3121. [CrossRef]
61. Titiš, J.; Miklovič, J.; Boča, R. Magnetostructural Study of Tetracoordinate Cobalt(II) Complexes. *Inorg. Chem. Commun.* **2013**, *35*, 72–75. [CrossRef]
62. Criado, J.J.; Jimenez-Sanchez, A.; Cano, F.H.; Saez-Puche, R.; Rodríguez-Fernandez, E. Preparation and characterization of tetrachlorocobaltates(II) of α,ω-alkylenediammonium. Magnetic and thermal properties. Crystal structure of $[NH_3(CH_2)_5NH_3]CoCl_4$. *Acta Crystallogr. Sect. B Struct. Sci. Cryst. Eng. Mater.* **1999**, *5*, 947–952. [CrossRef]
63. Liu, J.-J.; Jiang, S.-D.; Neugebauer, P.; van Slageren, J.; Lan, Y.; Wernsdorfer, W.; Wang, B.-W.; Gao, S. Magnetic and HFEPR Studies of Exchange Coupling in a Series of μ-Cl Dicobalt Complexes. *Inorg. Chem.* **2017**, *56*, 2417–2425. [CrossRef]

64. Protsenko, A.N.; Shakirova, O.G.; Protsenko, A.E.; Kuratieva, N.V.; Fowles, S.M.; Turnbull, M.M. Effect of isomeric cations of 3(2)-(chloromethyl)pyridine on the structure and properties of copper(II) and cobalt(II) complexes. *J. Mol. Struct.* **2021**, *1240*, 130561. [CrossRef]
65. Garci, F.; Chebbi, H.; Rouzbeh, N.; Rochels, L.; Disch, S.; Klein, A.; Faouzi Zid, M. Structure, optical and magnetic properties of the pyridinium cobaltate $(C_6H_9N_2)_2[CoCl_4]$. *Inorg. Chim. Acta* **2022**, *539*, 121003. [CrossRef]
66. Issaoui, F.; Amamou, W.; Bekri, M.; Zouari, F.; Dhahri, E.; Valente, M.A. Structural, magnetic and vibrational characterization of the new organic-inorganic hybrid material, $(C_9H_{14}N)_2CoCl_4$. *J. Mol. Struct.* **2019**, *1189*, 175–180. [CrossRef]
67. Pietrzyk, P.; Srebro, M.; Radoń, M.; Sojka, Z.; Michalak, A. Spin Ground State and Magnetic Properties of Cobalt(II): Relativistic DFT Calculations Guided by EPR Measurements of Bis(2,4-acetylacetonate)cobalt(II)-Based Complexes. *J. Phys. Chem. A* **2011**, *115*, 2316–2324. [CrossRef]
68. Ferjani, H.; Bechaeib, R.; Gil, D.M.; Klein, A. The 1D Hybrid Material Allylimidazolium Iodoantimonate: A Combined Experimental and Theoretical Study. *Inorganics* **2025**, *13*, 243. [CrossRef]
69. Figgis, B.N.; Hitchman, M.A. *Ligand Field Theory and Its Applications*; Wiley-VCH: New York, NY, USA, 2000.
70. Klein, A.; Elmas, S.; Butsch, K. Oxido Pincer Ligands—Exploring their Coordination Chemistry of Bis(hydroxymethyl)pyridine Ligands for the Late Transition Metals. *Eur. J. Inorg. Chem.* **2009**, *2009*, 2271–2281. [CrossRef]
71. Makuła, P.; Pacia, M.; Macyk, W. How to Correctly Determine the Band Gap Energy of Modified Semiconductor Photocatalysts Based on UV–Vis Spectra. *J. Phys. Chem. Lett.* **2018**, *9*, 6814–6817. [CrossRef]
72. Mukund, V.; Saddala, M.S.; Farran, B.; Mannavarapu, M.; Alam, A.; Nagaraju, G.P. Molecular docking studies of angiogenesis target protein HIF-1$\alpha$ and genistein in breast cancer. *Gene* **2019**, *701*, 169–172. [CrossRef]
73. Tang, X.; Lu, J.; Chen, H.; Zhai, L.; Zhang, Y.; Lou, H.; Wang, Y.; Sun, L.; Song, B. Underlying Mechanism and Active Ingredients of *Tianma Gouteng* Acting on Cerebral Infarction as Determined via Network Pharmacology Analysis Combined with Experimental Validation. *Front. Pharmacol.* **2021**, *12*, 760503. [CrossRef]
74. He, Y.; Diao, S.; Hou, S.; Li, T.; Meng, W.; Zhang, J. Identification of novel potential hypoxia-inducible factor-1$\alpha$ inhibitors through machine learning and computational simulations. *Front. Chem.* **2025**, *13*, 1585882. [CrossRef]
75. Riccardi, L.; Genna, V.; De Vivo, M. Metal–ligand interactions in drug design. *Nat. Rev. Chem.* **2018**, *2*, 100–112. [CrossRef]
76. Lee, K.; Kang, J.E.; Park, S.-K.; Jin, Y.; Chung, K.-S.; Kim, H.-M.; Lee, K.; Kang, M.R.; Lee, M.K.; Song, K.B.; et al. LW6, a novel HIF-1 inhibitor, promotes proteasomal degradation of HIF-1$\alpha$ via upregulation of VHL in a colon cancer cell line. *Biochem. Pharmacol.* **2010**, *80*, 982–989. [CrossRef]
77. Esakkimuthukumar, M.; Swaroop, A.K.; Patnaik, S.K.; Kumar, R.R.; Praveen, T.K.; Naik, M.R.; Selvaraj, J. A novel family of small molecule HIF-1 alpha stabilizers for the treatment of diabetic wounds; an integrated in silico, in vitro, and in vivo strategy. *RSC Adv.* **2022**, *12*, 31293–31302. [CrossRef]
78. Lueken, H.; Schilder, H.; Eifert, T.; Handrick, K.; Hüning, F. Magnetochemistry: Compounds and Concepts. In *Advances in Solid State Physics*; Kramer, B., Ed.; Springer: Berlin/Heidelberg, Germany, 2001; Volume 41. [CrossRef]
79. *APEX4—Software Suite for Crystallographic Programs*; Bruker AXS, Inc.: Madison, WI, USA, 2021.
80. Sheldrick, G.M. SHELXT—Integrated space-group and crystal-structure determination. *Acta Crystallogr. A Found. Adv.* **2015**, *71*, 3–8. [CrossRef]
81. Sheldrick, G.M. A short history of SHELX. *Acta Crystallogr. A Found. Adv.* **2008**, *64*, 112–122. [CrossRef] [PubMed]
82. Sheldrick, G.M. Crystal structure refinement with SHELXL. *Acta Crystallogr. C Struct. Chem.* **2015**, *71*, 3–8. [CrossRef] [PubMed]
83. Spackman, P.R.; Turner, M.J.; McKinnon, J.J.; Wolff, S.K.; Grimwood, D.J.; Jayatilaka, D.; Spackman, M.A. CrystalExplorer: A Program for Hirshfeld Surface Analysis, Visualization and Quantitative Analysis of Molecular Crystals. *J. Appl. Crystallogr.* **2021**, *54*, 1006–1011. [CrossRef] [PubMed]
84. Spackman, M.A.; Byrom, P.G. A Novel Definition of a Molecule in a Crystal. *Chem. Phys. Lett.* **1997**, *267*, 215–220. [CrossRef]
85. McKinnon, J.J.; Spackman, M.A.; Mitchell, A.S. Novel Tools for Visualizing and Exploring Intermolecular Interactions in Molecular Crystals. *Acta Crystallogr. Sect. B Struct. Sci. Crystal Engin. Mater.* **2004**, *60*, 627–668. [CrossRef]
86. Wood, P.A.; McKinnon, J.J.; Parsons, S.; Pidcock, E.; Spackman, M.A. Analysis of the Packing of Organic Molecules Using Hirshfeld Surfaces. *CrystEngComm* **2008**, *10*, 368–376.
87. Frisch, M.J.; Trucks, G.W.; Schlegel, H.B.; Scuseria, G.E.; Robb, M.A.; Cheeseman, J.R.; Scalmani, G.; Barone, V.; Petersson, G.A.; Nakatsuji, H.; et al. *Gaussian 16*; Revision C.01; Gaussian, Inc.: Wallingford, CT, USA, 2016.
88. Adamo, C.; Barone, V. Toward Reliable Density Functional Methods without Adjustable Parameters: The PBE0 Model. *J. Chem. Phys.* **1999**, *110*, 6158–6170. [CrossRef]
89. Grimme, S.; Antony, J.; Ehrlich, S.; Krieg, H. A Consistent and Accurate Ab Initio Parametrization of Density Functional Dispersion Correction (DFT-D) for the 94 Elements H-Pu. *J. Chem. Phys.* **2010**, *132*, 154104. [CrossRef]
90. Miertuš, S.; Scrocco, E.; Tomasi, J. Electrostatic Interaction of a Solute with a Continuum. A Direct Utilization of AB Initio Molecular Potentials for the Prevision of Solvent Effects. *Chem. Phys.* **1981**, *55*, 117–129. [CrossRef]

91. Bacskay, G.B. A Quadratically Convergent Hartree—Fock (QC-SCF) Method. Application to Closed Shell Systems. *Chem. Phys.* **1981**, *61*, 385–404. [CrossRef]
92. O'boyle, N.M.; Tenderholt, A.L.; Langner, K.M. cclib: A Library for Package-Independent Computational Chemistry Algorithms. *J. Comput. Chem.* **2008**, *29*, 839–845. [CrossRef]
93. Lu, T. A Comprehensive Electron Wavefunction Analysis Toolbox for Chemists, Multiwfn. *J. Chem. Phys.* **2024**, *161*, 082503. [CrossRef]
94. Hirshfeld, F.L. Bonded-Atom Fragments for Describing Molecular Charge Densities. *Theor. Chim. Acta* **1977**, *44*, 129–138. [CrossRef]
95. Morris, G.M.; Huey, R.; Lindstrom, W.; Sanner, M.F.; Belew, R.K.; Goodsell, D.S.; Olson, A.J. AutoDock4 and AutoDockTools4: Automated docking with selective receptor flexibility. *J. Comput. Chem.* **2009**, *30*, 2785–2791. [CrossRef] [PubMed]
96. Waterhouse, A.; Bertoni, M.; Bienert, S.; Studer, G.; Tauriello, G.; Gumienny, R.; Heer, F.T.; de Beer, T.A.P.; Rempfer, C.; Bordoli, L.; et al. SWISS-MODEL: Homology modelling of protein structures and complexes. *Nucleic Acids Res.* **2018**, *46*, W296–W303. [CrossRef] [PubMed]
97. BIOVIA, Dassault Systèmes, Discovery Studio Visualizer, Version 20.1.0.19295 SDDS 2020. Available online: https://discover.3ds.com/discovery-studio-visualizer-download (accessed on 2 October 2025).